

The ISOPHOT 170 μm serendipity survey

I. Compact sources with galaxy associations*

M. Stickel¹, D. Lemke¹, U. Klaas¹, C.A. Beichman², M. Rowan-Robinson³, A. Efstathiou³, S. Bogun⁴, M. F. Kessler⁵, and G. Richter⁶

¹ Max-Planck-Institut für Astronomie, Königstuhl 17, 69117 Heidelberg, Germany

² Infrared Processing and Analysis Center, JPL, California Institute of Technology, MS 100/22, Pasadena, CA 91125, USA

³ Imperial College of Science, Technology and Medicine, The Blackett Laboratory, Prince Consort Road, London SW7 2BZ, UK

⁴ Data Management and Operations Division, ESO, Karl-Schwarzschild-Strasse 2, 85748 Garching bei München, Germany

⁵ ISO Data Centre, Astrophysics Division, Space Science Department of ESA, Villafranca, P.O. Box 50727, 28080 Madrid, Spain

⁶ Astrophysikalisches Institut Potsdam, An der Sternwarte 16, 14482 Potsdam, Germany

Received 16 February 2000 / Accepted 9 May 2000

Abstract. The first set of compact sources observed in the ISOPHOT 170 μm Serendipity Survey is presented. From the slew data with low ($I_{100\mu\text{m}} \leq 15 \text{ MJy/sr}$) cirrus background, 115 well-observed sources with a high signal-to-noise ratio in all detector pixels having a galaxy association were extracted. Of the galaxies with known optical morphologies, the vast majority are classified as spirals, barred spirals, or irregulars. The 170 μm fluxes measured from the Serendipity slews have been put on an absolute flux level by using calibration sources observed additionally with the photometric mapping mode of ISOPHOT. For all but a few galaxies, the 170 μm fluxes are determined for the first time, which represents a significant increase in the number of galaxies with measured Far-Infrared (FIR) fluxes beyond the IRAS 100 μm limit. The 170 μm fluxes cover the range $2 \lesssim F_{170\mu\text{m}} \lesssim 100 \text{ Jy}$. Formulae for the integrated FIR fluxes $F_{40-220\mu\text{m}}$ and the total infrared fluxes $F_{1-1000\mu\text{m}}$ incorporating the new 170 μm fluxes are provided. The large fraction of sources with a high $F_{170\mu\text{m}}/F_{100\mu\text{m}}$ flux ratio indicates that a cold ($T_{\text{Dust}} \lesssim 20 \text{ K}$) dust component is present in many galaxies. The detection of such a cold dust component is crucial for the determination of the total dust mass in galaxies, and, in cases with a large $F_{170\mu\text{m}}/F_{100\mu\text{m}}$ flux ratio, increases the dust mass by a significant factor. The typical mass of the coldest dust component is $M_{\text{Dust}} = 10^{7.5 \pm 0.5} M_{\odot}$, a factor 2–10 larger than that derived from IRAS fluxes alone. As a consequence, the majority of the derived gas-to-dust ratios are much closer to the canonical value of ≈ 160 for the Milky Way. By relaxing the selection cri-

teria, it is expected that the Serendipity Survey will eventually lead to a catalog of 170 μm fluxes for ≈ 1000 galaxies.

Key words: methods: data analysis – catalogs – surveys – galaxies: ISM – infrared: galaxies

1. Introduction

While there is general agreement that the far infrared (FIR) emission of normal galaxies is due to the thermal radiation from dust grains distributed in the interstellar medium, still a debated issue is whether a cold dust component with temperatures of 15–20 K is present in the majority of galaxies. It would most easily be discernible by an increasing flux at FIR wavelengths beyond 100 μm and would contribute the bulk of the FIR flux.

Although such a cold dust component can in general also be inferred from an excess over the extrapolated coldest FIR blackbody at sub-mm wavelengths, measurements near the peak of the spectral energy distribution (SED) between 100 μm and 200 μm are crucial for the correct decomposition of the FIR and sub-mm data. This has been exemplified by Chini et al. (1995), where a given sub-mm flux can either be reconciled with a 15–20 K dust component dominating the FIR SED between 100 μm –200 μm or equally well with a much weaker component from even colder dust in conjunction with a much warmer dust component. Moreover, estimates of the dust temperature, and hence dust mass, based on the IRAS 60 μm and 100 μm fluxes alone are extremely unreliable, as the 60 μm flux can be dominated by emission from transiently heated small particles (Mathis 1990).

Up to now, only a small number of galaxies have been investigated at these FIR wavelengths either individually in some detail (Smith 1982; Klaas et al. 1997; Haas et al. 1998; Haas 1998), or as groups of several objects (Stark et al. 1989; Alton et al. 1998; Krügel et al. 1998; Odenwald et al. 1998; Perez Garcia et al. 1998; Siebenmorgen et al. 1999). However,

Send offprint requests to: M. Stickel

* Based on observations with ISO, an ESA project with instruments funded by ESA Member States (especially the PI countries: France, Germany, the Netherlands and the United Kingdom) and with the participation of ISAS and NASA. Members of the Consortium on the ISOPHOT Serendipity Survey (CISS) are MPIA Heidelberg, ESA ISO SOC Villafranca, AIP Potsdam, IPAC Pasadena, Imperial College London

Correspondence to: stickel@mpia-hd.mpg.de

for the study of the frequency of a cold dust component and its correlation with other properties of the galaxies, a much larger sample is needed.

In using the slewing time of the Infrared Space Observatory (ISO; Kessler et al. 1996) for scientific observations, the ISOPHOT (Lemke et al. 1996) Serendipity slew survey (Bogun et al. 1996) was designed to be particularly suitable for studying the FIR emission of galaxies beyond the IRAS 100 μ m wavelength limit. The prohibitively long observation time required for pointed photometric observations of a large galaxy sample is avoided by carrying out a survey during otherwise unused telescope time over as large a fraction of the sky as possible using a single wavelength near the expected peak of the SED. The ISOPHOT Serendipity Survey is the only large scale survey covering a significant fraction of the sky at 170 μ m. The development of the source extraction methods and initial scientific results of the Serendipity Survey have been described by (Stickel et al. 1998a,b, 1999).

Here we present the first set of well-observed, almost centrally crossed compact sources associated with known galaxies extracted from the strip scanning measurements. This paper is intended to be first in a series, where in future papers the current rather stringent selection criteria will be relaxed, e.g. by including compact sources with known galaxy associations not centrally crossed, and by including compact sources without known galaxy associations. This will eventually lead to the final catalog of compact Serendipity Survey sources.

2. Observations and data reduction

Serendipity slew survey measurements were acquired with the ISOPHOT C200 detector (Lemke et al. 1996), a 2×2 pixel array of stressed Ge:Ga with a pixel size of $89''.4$, which was used in conjunction with the C_160 broad band filter (reference wavelength 170 μ m, equivalent width 89 μ m). The high dynamic range of sky brightness between the galactic plane and the galactic poles together with the slew speed of the telescope (max. $\approx 8' s^{-1}$) required the fastest uncompressed read-out rate of the C200 camera of 1/8 s reset interval time, during which four detector read-outs took place. During the lifetime of the ISO mission, about 550 hours of measurements have been gathered with more than 12000 slews. The total slew length exceeds 150000° resulting in a sky coverage of $\approx 15\%$.

For each detector pixel, the raw data consist of detector voltages as a function of read-out time. The conversion to slew surface brightnesses followed standard data reduction techniques within the ISOPHOT Interactive Analysis PIA¹ (Gabriel et al. 1997) Version 7.2 software package. Surface brightnesses are derived from the fitted read-out ramp slopes either by using a measurement of the on-board Fine Calibration Source (FCS) preceding the slew observation, or, for short slews, by using the default C200 calibration.

¹ The ISOPHOT data presented in this paper were reduced using PIA, which is a joint development by the ESA Astrophysics Division and the ISOPHOT Consortium. The ISOPHOT Consortium is led by the Max-Planck-Institute for Astronomy, Heidelberg.

Table 1. ISOPHOT Serendipity Slew Processing Steps

1	Conversion of raw detector read-out data streams to surface brightnesses
2	Subtraction of large scale background
3	Removal of one-sample wide cosmic ray hits
4	Phase-shifted averaging of background-subtracted pixel data streams
5	Identification of source candidates as peaks higher than 3σ of local noise
6	Determination of source offset perpendicular to slew
7	Source fitting with two-dimensional gaussian with fixed slew offset

During slewing the nominal telescope pointing information was delivered by the on-board gyros alone. Gyro drifts, i.e. offsets between nominal and actual sky positions increasing with slewing time, were recognized by the difference between these two positions at the end of a slew, where the accurate telescope position at the next target was provided by the star-trackers. Assuming that the gyro drift is a linear function of cumulative slewing angle, this offset was used to correct all gyro positions along the slew.

The Serendipity slew data consist of very narrow stripes across the sky, lacking, to first approximation, practically any redundancy. Furthermore, fluxes can not be derived from the one-dimensional data stream alone, because sources will be crossed with arbitrary slew velocities, impact parameters, and detector position angles, where the detector pixels not necessarily sample the central peak of a source. Data analysis (summarized in Table 1) will have to make use at least in parts of a two-dimensional reconstruction and analysis of the source profiles.

The first step to search for source candidates lying on the slews was the determination and subtraction of the large scale background from diffuse galactic emission and extended galactic cirrus structures. To avoid loss of resolution, the flux calibrated data streams of the four pixels are not rebinned, but kept as a function of signal number. After denoising with a non-linear filter (Smith & Brady 1997), a morphological rolling ball algorithm (Sternberg 1986) was applied to remove all peaks up to a width somewhat larger than that of point sources. The full width at zero intensity for point sources was chosen to be five times the FWHM ($57''$) of a gaussian approximation to the C200 170 μ m beam profile. Because of the variable slew speed, the size of the rolling ball, as measured in number of signals, was not constant along the slew.

Cosmic ray hits (glitches) were removed from the individual background subtracted data streams of the four pixels by using a noise peak elimination filter (Imme 1991), where data points were replaced only if they were confined to one signal and exceeded the local noise level by a factor of three. Very high one signal wide peaks in the center of sources may have erroneously be removed by this procedure, but this was undone

by copying back the signals in question once a source region had been identified.

The deglitched and background subtracted signals of the four pixels were phase-shifted according to the position angle of the detector and a signal-to-noise ratio weighted averaged signal was derived. The resulting mean signal was again slightly filtered (Smith & Brady 1997), from which regions of source candidates were selected by setting a cut on the filtered mean surface brightness. This cut was set to 3σ of the local noise level, which in turn was non-constant due to crossing of the regions with different background levels such as the galactic plane. No other criterion such as a detection with a predefined signal-to-noise ratio in several pixels was required for the definition of a source candidate region. The low threshold for the source candidate selection guarantees that even faint sources will be found. On the other hand, this obviously leads to quite a number of false faint source candidates, mostly unremoved detector hits by cosmic rays, which, however, can easily be recognized because their widths are well below those expected for unresolved point sources.

The early Serendipity source extraction method had shown that fitting the source candidates with a full two-dimensional gaussian to derive both the position and the total source flux simultaneously was not always stable, leading occasionally to a run-away of the fit resulting in sources far-off the slew with apparently very high fluxes (Stickel et al. 1998a). Therefore, to decouple the determination of the position from the flux determination, the ratio of the four peak fluxes to the highest flux among the four pixels was used in comparison with the expected ratios from a gaussian source model to estimate the source position relative to the slew. With the position of the gaussian fixed, only the total source flux is derived from 2D gaussian fitting. This constituted a major processing improvement judging by the close agreement of flux values for repeatedly crossed sources.

The data processing is illustrated in Fig. 1, showing for ISOSS J 19083+5055 (NGC 6764, IRAS 19070+5051), the Serendipity slew data, the estimated background, the background subtracted and deglitched datastream together with the two-dimensional fit and the fit residuals. As the data for detector pixel 4 (rightmost) show, even cosmic ray hits lying very close to the source center can be removed quite effectively. The overall residuals after subtraction of the source fit hardly exceed the brightness variations away from the source even for pixel 1, which had seen the highest signal.

3. Calibration

To tie the fluxes derived from the Serendipity slews to an absolute photometric level, dedicated photometric calibration measurements of 12 sources repeatedly crossed with varying impact parameters were obtained with ISOPHOT. For six of them, these measurements consisted of raster maps (AOT P22; Klaas et al. 1994) of two different angular sizes with the C200 detector and C₁₆₀ broad band filter. For the larger maps the ramp integration time was set to 1/8 s, identical to that used during slewing. The raster step size between subsequent detec-

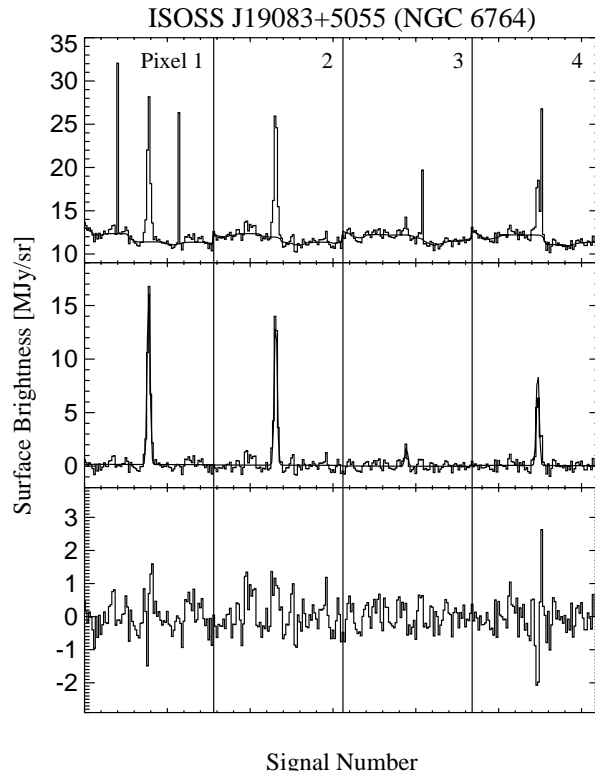


Fig. 1. Serendipity slew data ISOSS J 19083+5055 (NGC 6764, IRAS 19070+5051). Each panel shows the region around the source from all four detector pixels side-by-side. Top: Observed slew data showing in addition to the source centered in the window of each pixel several (except pixel 2) one signal wide cosmic ray hits. The continuous line below the source is the estimated background. Middle: The deglitched background subtracted datastream with the result of the two-dimensional gaussian source fit overlaid. Bottom: Residuals after subtraction of the fitted two-dimensional source model from the background subtracted, deglitched data stream.

tor positions on the sky was set to half a detector pixel ($45''$). For the smaller mini-maps, a raster step size of a full detector pixel was chosen, and the ramp integration time was adapted to the expected source flux. The remaining six sources were only observed with the latter mini-map set-up.

Basic data reduction of the calibration maps up to the flux calibrated data streams utilized the ISOPHOT interactive analysis package PIA. The actual maps were produced using the drizzle mapping method (Hook & Fruchter 1997) within IRAF². Integrated source fluxes were derived using ESO-MIDAS³ by summing up the source flux in boxes and subtracting an averaged background value from a source free region. Uncertainties in the mapping fluxes are $\approx 15\%$ for the brighter sources, and up

² IRAF is distributed by the National Optical Astronomy Observatories, which are operated by the Association of Universities for Research in Astronomy, Inc., under cooperative agreement with the National Science Foundation.

³ ESO-MIDAS is the acronym for the European Southern Observatory Munich Image Data Analysis System which is developed and maintained by the European Southern Observatory.

Table 2. ISOPHOT Serendipity Survey Calibration Sources

Name	Map flux [Jy]	Serend. Flux [Jy]
NGC 6140 (IRAS 16206+6530)	7.5	6.5, 5.2
NGC 6190 (IRAS 16312+5832)	3.4	2.9, 3.9
IRAS 16404+5910	2.3	2.5, 1.3
		1.4
IC 1228 (IRAS 16418+6540)	7.8	5.8, 8.9
		4.1
UGC 10559 (IRAS 16460+5910A)	3.8	2.6, 4.3
		4.6
NGC 6286 (IRAS 16577+5900)	25.0	15.7, 11.6
IRAS 17213+4814	2.1	1.0, 1.9
		2.0, 0.9
		1.1
NGC 6381 (IRAS 17266+6003) (ISSO #83)	3.9	2.9, 2.2
		4.1, 2.9
		2.9
NGC 6503 (IRAS 17499+7009) (ISSO #86)	44.5	24.9, 25.9
NGC 6543 (IC 4677) (IRAS 17584+6638)	27.4	13.2, 16.1
		19.6, 17.1
		16.4, 18.4
		19.5, 20.8
		17.2
NGC 6670 (IRAS 18329+5950) (ISSO #91)	13.1	11.2, 10.0
		9.2, 6.7
NGC 7674 (IRAS 23254+0830)	7.1	9.2, 7.3

Notes:

- ISSO sequence numbers in parantheses refer to the sequential source numbering in Table 4.
- Several Serendipity flux entries for a single source refer to different source crossings.
- Tabulated Serendipity slew fluxes are not corrected for signal losses.

to $\approx 30\%$ for the fainter sources, as derived from several combinations of source and background regions for each individual source.

The final photometric fluxes are listed in Table 2, together with the Serendipity Survey fluxes derived from the slews. The ratio of Serendipity Survey and mapping fluxes as a function of the mapping fluxes is shown in Fig. 2. It indicates that for the brighter sources the slewing observations miss some signal due to transient effects in the detector output (Acosta-Pulido et al. 2000). For the fainter sources the ratio shows a significantly increased scatter, which can be understood as the influence of the noise on the observed brightness distribution of the four detector pixels.

To correct for the signal loss during slewing, the Serendipity slew fluxes will subsequently be scaled by the linear relationship shown as a dashed line in Fig. 2. This is a fit to all data points with serendipity mode to photometric flux ratios between 0.5 and 1.2, excluding the gross outliers. Its intercept is close to 0.9, which means that the faintest sources will not significantly

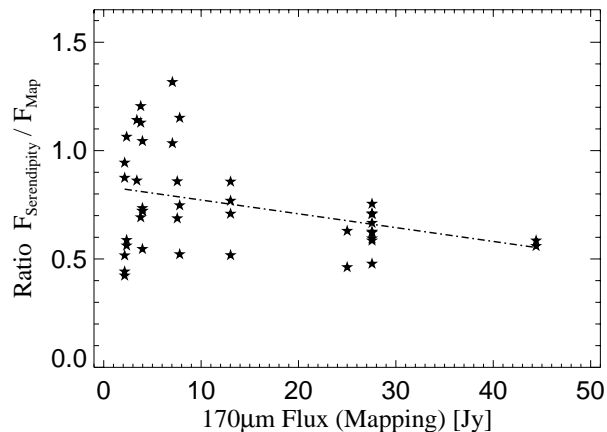


Fig. 2. The ratio of photometric mapping and Serendipity slew fluxes vs. the photometric flux for all repeated crossings of the 12 calibration sources. For the brighter sources, the Serendipity slews miss some flux. At the faint end an increased scatter is noticeable, most likely due to the influence of noise on the slew fluxes. The dashed line shows the linear relationship used to correct the source fluxes derived from the slews. Except for the faint end, the agreement between repeated slew observations is $\lesssim 40\%$.

be scaled. At the bright end, it reaches the ratio of ≈ 0.5 for a photometric flux of ≈ 60 Jy, corresponding to a slew flux of ≈ 30 Jy. The scatter of the flux ratios in Fig. 2 indicates an overall photometric accuracy of the corrected source fluxes of $\lesssim 40\%$.

To avoid an extrapolation of the scaling factor, thereby possibly artificially increasing the 170 μ m fluxes, all sources with slew fluxes above ≈ 30 Jy will be corrected by a constant scaling factor of 2. This does not represent a major drawback, since the brightest sources are nearby galaxies with very small redshifts and thus have probably apparent diameters larger than the detector size, where the slewing in any case can not give a good measure of the total source flux. A correction factor of ≈ 2 even for the very brightest sources is corroborated by a slew measurement of the nearby galaxy NGC 6946, which gives an uncorrected Serendipity flux of ≈ 300 Jy, while the total 200 μ m flux derived from ISOPHOT mapping observations is 743 Jy (Alton et al. 1998). The agreement is even more remarkable in view of the large apparent optical diameter of $\approx 10'$ of NGC 6946, which is reflected also in the slew data with a fitted width of $\sigma \approx 2'$.

4. The catalog

This initial Serendipity source list is intended to cover only the most reliable extragalactic sources. The final set of sources described below is regarded to be unbiased and representative of the much larger number of galaxies crossed by the ISOPHOT Serendipity slews.

The Serendipity source candidate database was searched for sources where a peak with a signal-to-noise ratio of at least 5 had been seen in the data streams of all four detector pixels. Although the background determination was designed to keep preferentially compact sources in the background sub-

Table 3. Galaxy Selection Criteria

1	Signal-to-noise ratio > 5 in all four detector pixels
2	Fitted two-dimensional gaussian width $0.5' \leq \sigma \leq 1.25'$
3	Background in $1 \square^\circ$ IRAS/COBE $100 \mu\text{m}$ field $\leq 15 \text{ MJy/sr}$
4	Galactic latitudes $ b > 15^\circ$
5	Galaxy association (optical diameter $< 6'$) within $3'$

tracted data streams, only sources with a fitted gaussian width of $0.5' \leq \sigma \leq 1.25'$ were considered. The lower cutoff also rejects any residual glitches quite effectively. Since narrow cirrus structures can still be mistaken for compact sources, we tried to minimize cirrus confusion by removing all source candidates where the mode of the pixel brightnesses in a $1 \square^\circ$ field extracted from the IRAS/COBE $100 \mu\text{m}$ maps (Schlegel et al. 1998) centered on the source candidates exceeded 15 MJy/sr . The selection was further restricted to galactic latitudes $|b| > 15^\circ$. Only sources were considered where the NED and/or SIMBAD databases listed an association classified as a galaxy with an optical diameter $< 6'$ within $3'$ from the Serendipity source position. Eventually, remaining chance associations of compact cirrus structures predominantly with fainter galaxies were discarded by an eye-ball check of the one-dimensional slew brightnesses at 100 and $170 \mu\text{m}$, the former of which had been extracted from the IRAS/ISSA $100 \mu\text{m}$ maps, and the appearance of the source candidates on the two-dimensional IRAS/ISSA $100 \mu\text{m}$ maps. A summary of the selection criteria are given in Table 3.

The final source list is given in Table 4, which lists in Column 1 a sequence number and in Column 2 the ISOPHOT Serendipity Survey source designation, derived from the J2000 source position. Since it is anticipated that the Serendipity slew measurements will eventually lead to a database of compact galactic and extragalactic sources containing several thousand objects, the source designation was registered with the IAU Commission 5 Task Group on Designations. The proposed acronym specifying the collection of sources is ISOSS, for ISOPHOT Serendipity Survey. The sources of the ISOSS catalog are uniquely determined with a coordinate-based designation similar to the IRAS convention, namely HHMMm+DDMM, where the rightmost digit of the right ascension is the truncated decimal part of the right ascension minutes.

Table 4 is continued with the galaxy name from a major optical galaxy catalog (Column 3), the fitted J2000 source position from the Serendipity slews (Column 4,5), the Serendipity $170 \mu\text{m}$ flux (Column 6) and its associated formal fit error (Column 7), the IRAS FSC $100 \mu\text{m}$ and $60 \mu\text{m}$ fluxes (Column 8,9 Moshir et al. 1992), the IRAS FSC Cirrus flag (Column 10 Moshir et al. 1992), the fitted Serendipity gaussian source width (Column 11), the source offset perpendicular to the slew (Column 12), the average $170 \mu\text{m}$ background underneath the source (Column 13), the optical classification (Column 14), the optical brightness (Column 15), and the redshift (Column 16). The latter optical and redshift information was almost exclusively taken from NED, supplemented by three redshifts from the PSCz cat (Saunders et al. 2000) as described in the notes to Table 4. Two galaxies (ISOSS J00434–5011 = NGC 0238,

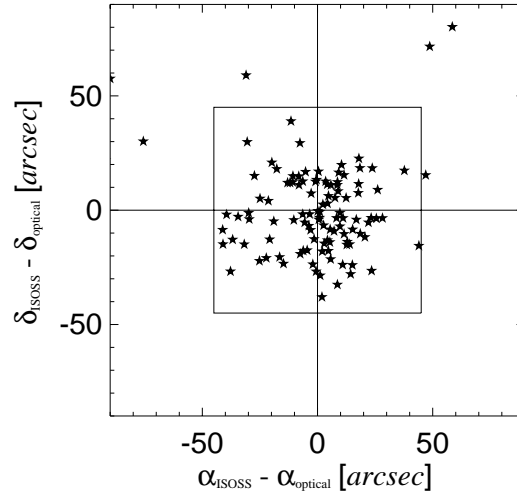


Fig. 3. The differences of the rightascension and declination coordinates between the ISOSS and the optical positions for the galaxies from Table 4. The vast majority is confined to a region of $90'' \times 90''$, the C200 pixel size.

ISOSS J21482+2209 = NGC 7137) are not listed in the IRAS FSC, but both are present on the IRAS ISSA plates. Accordingly, no $60 \mu\text{m}$ and $100 \mu\text{m}$ fluxes are available, as indicated by the value -1 in Table 4. Both galaxies lie close to the border of the sky regions not observed by IRAS and have only a single coverage, which was insufficient for an inclusion in the IRAS FSC.

For galaxies with known Hubble types, the prevalence of spirals is striking. Only one is actually of an intermediate elliptical/disk type (ISOSS J00152–2402 = MCG $-04 - 01 - 027$), while there are roughly equal numbers of S, SA, SAB, and SB type galaxies, a few of which also carry an activity indicator such as Sy or LINER. There are only three galaxies with a classification as irregulars, one of which is questionable.

5. Source sample properties

5.1. Positions

The high-quality Serendipity Survey sources selected for this first investigation are particularly well suited to check the combined positional accuracy which can be reached with the large C200 pixel size, the above mentioned gyro drift correction, and the method employed to derive source positions relative to the slews as described above. Fig. 3 shows the offsets between the ISOSS coordinates and the optical coordinates extracted from the NED database for all galaxies from Table 4. The distribution is highly concentrated towards zero right ascension and declination offsets. More than 90% lie within a circle with $45''$ radius. Only 10 sources lie outside the central area of $90'' \times 90''$ (C200 pixel size), while 4 of which are actually outside the plotted range, but closer than $2'$ to the origin. Although these latter outliers are all located towards the end of long slews, a much larger group of sources with gross coordinate offsets are needed to investigate a possible common cause for this result.

Table 4. Compact ISOPHOT serendipity sources with associated galaxies*

Seq.	Designation	other Name	α_{2000}	δ_{2000}	$F_{170\mu\text{m}}$	$\Delta_{170\mu\text{m}}$	$F_{100\mu\text{m}}$	$F_{60\mu\text{m}}$	Cirr.	Width	Offset	$B_{170\mu\text{m}}$	Classification	m	z
(1)	(2)	(3)	[h m s]	[d m s]	[Jy]	[Jy]	[Jy]	[Jy]	(10)	[']	[']	[MJy/sr]	(14)	[mag]	[km/s]
1	00052-1629	NGC 7821	00 05 17	-16 29 03	6.93	0.38	6.58	2.67	3	1.16	0.33	5.78	Scd pec sp	13.77	7339
2	00152-2402	MCG -04-01-027	00 15 15	-24 02 39	4.36	2.11	3.05	1.27	2	1.09	0.33	5.05	SA(s)0/E2	15.18	7572
3	00159-1606	UGC 00148	00 15 54	+16 06 32	6.53	0.39	5.04	2.21	2	0.89	0.42	11.62	S?	14.09	4213
4	00347-0823	NGC 0157	00 34 47	-08 23 42	92.72	3.62	39.49	13.32	0	1.09	0.08	7.36	SAB(rs)bc	11.00	1668
5	00434-5011	NGC 238	00 43 26	-50 11 07	3.40	0.93	-1.00	-1.00	-1	0.75	0.17	4.41	SB(rs)b	13.14	8596
6	00577-2730	MCG -05-03-020	00 57 47	-27 30 14	6.91	0.33	2.94	0.60	1	0.83	0.75	7.47	SAB(r)c	13.58	5609
7	01163+4644	UGC 00816	01 16 21	+46 44 36	6.25	0.35	6.25	2.85	0	1.00	0.58	8.41	Sc/Sb	14.2	5188
8	01213+4029	NGC 0477	01 21 18	+40 29 19	4.50	0.36	2.56	1.09	2	1.09	0.50	9.10	SAB(s)c	13.70	5876
9	01245+0347	NGC 0520	01 24 35	+03 47 28	62.62	2.30	45.81	30.87	1	0.84	1.00	14.34	S pec	12.4	2265
10	01254-3816	NGC 0549	01 25 29	-38 16 06	3.23	0.12	1.52	0.54	1	0.66	0.25	5.48	Sab	14.79	6176
11	01373-6453	NGC 0646	01 37 22	-64 53 29	5.90	0.30	6.65	2.82	0	0.73	0.08	4.70	—	14.24	8230
12	01400-2841	MCG -05-05-007	01 40 00	-28 41 34	4.80	1.33	1.64	0.42	0	1.09	0.33	5.74	Sbc	13.42	5904
13	02039-1940	UGC 01560	02 03 54	+19 40 02	3.08	0.38	3.12	1.42	7	0.75	0.25	14.00	SB(s)b	14.56	8491
14	02107-7502	ESO 030- G 009	02 10 42	-75 02 52	2.18	0.40	1.18	0.26	0	0.90	0.25	6.35	SAB(rs)b	14.27	8133
15	02250+2212	UGC 01871	02 25 05	+22 12 59	8.98	0.48	8.76	3.70	0	0.63	0.25	17.59	S?	14.87	10121
16	02462+1305	UGC 02238	02 46 17	+13 05 37	16.05	0.53	15.28	7.70	0	0.81	0.25	13.82	Im?	14.61	6436
17	02464-0029	NGC 1087	02 46 27	-00 29 58	74.94	0.98	27.30	12.23	2	0.95	1.08	10.49	SAB(rs)c	11.46	1519
18	02480-1357	NGC 1103	02 48 03	-13 57 46	6.27	0.64	5.17	1.82	0	1.00	0.08	4.69	SB(s)b	13.61	4138
19	03198-2603	NGC 1302	03 19 49	-26 03 58	4.20	0.46	1.74	0.26	2	1.00	0.25	4.03	SAB(r)la	11.69	1703
20	04213-1848	MCG -03-12-002	04 21 20	-18 48 43	6.59	0.37	8.20	5.75	1	0.84	0.17	6.44	LINER	15.24	9652
21	04228-4738	ESO 042123-4745.1	04 22 51	-47 38 35	1.88	0.44	1.35	0.41	1	1.01	0.25	4.90	S	16.06	—
22	04309+0532	UGC 03066	04 30 57	+05 32 54	5.88	0.39	3.23	0.95	1	0.91	0.50	31.92	SAB(r)d	14.46	4639
23	04340-0834	NGC 1614	04 34 00	-08 34 57	17.12	0.67	32.69	32.31	3	0.79	0.17	17.87	SB(s)c pec;HII;Sy2	13.63	4778
24	04486-0619	NGC 1667	04 48 36	-06 19 35	20.81	1.35	14.73	5.95	4	0.78	0.42	11.72	SAB(r)c;Sy2	12.77	4546
25	05015-1609	MCG -03-13-051	05 01 30	-16 09 43	6.80	0.77	3.01	0.95	0	0.98	0.33	14.61	SB(s)b	14	6640
26	05054-4933	NGC 1803	05 05 28	-49 33 57	8.22	0.42	7.88	3.07	1	0.90	0.42	4.21	Sbc	13.38	4085
27	05146-1426	NPM1G -14.0236	05 14 41	-14 26 46	2.54	0.39	2.71	0.94	3	0.80	0.08	16.61	—	16.48	11040
28	05215-2614	AM 0519-261	05 21 31	-26 14 30	3.21	0.23	3.11	1.59	1	1.02	0.17	5.74	S?	—	13371
29	05467-1646	NGC 2076	05 46 46	-16 46 44	48.59	1.06	19.88	6.70	0	0.82	1.00	14.56	S0+; sp	14.0	2142
30	07453-7124	NGC 2466	07 45 23	-71 24 13	6.02	1.85	10.42	3.30	0	0.95	1.08	22.55	SA(s)c	13.54	5313
31	08556-7813	NGC 2655	08 55 39	+78 13 01	12.81	0.60	4.98	1.67	1	0.97	0.67	8.41	SAB(s)0/a;Sy2	10.96	1404
32	09066-7549	ESO 090701-7536.3	09 06 39	-75 49 40	12.90	0.54	9.76	3.42	0	0.74	0.50	16.16	SAB(rs)c	13.73	4630
33	09406+1153	NGC 2958	09 40 41	+11 53 29	5.24	0.30	3.12	1.24	2	0.88	0.25	5.80	S(r)bc	13.97	6663
34	10033+6843	NGC 3077	10 03 18	+68 43 41	25.37	0.79	26.43	13.65	1	0.83	0.25	8.92	I0 pec	10.61	14
35	10135+2243	NGC 3162	10 13 32	+22 43 44	12.38	0.38	6.81	2.48	2	0.85	0.83	6.48	SAB(rs)bc	12.21	1298
36	10218+7410	NGC 3183	10 21 52	+74 10 18	10.72	0.39	9.97	3.35	1	0.79	0.08	6.56	SB(s)b	12.68	3088
37	10270-3613	MCG -06-23-029	10 27 04	-36 13 48	5.33	0.41	4.69	2.13	1	0.78	0.25	7.93	Sbc; sp	14.52	3122
38	11527+4408	NGC 3938	11 52 46	+44 08 12	40.42	0.03	23.06	5.86	0	1.18	1.25	4.54	SA(s)c	10.90	809
39	12055+5032	NGC 4088	12 05 32	+50 32 42	144.78	2.54	54.47	19.88	1	1.25	1.33	6.68	SAB(rs)bc	11.15	759
40	12127+1051	NGC 4178	12 12 46	+10 51 43	15.42	0.46	8.08	2.11	3	0.83	0.08	6.39	SB(rs)dm	11.90	378
41	12163+1318	NGC 4222	12 16 22	+13 18 41	5.88	0.21	3.19	0.99	0	0.86	0.58	7.02	Sc	13.86	230
42	12212-1823	NGC 4293	12 21 12	-18 23 09	11.88	0.42	10.44	4.58	0	0.89	0.42	6.39	SB(s)0/a	11.26	893
43	12254+1628	NGC 4383	12 25 26	+16 28 09	17.86	0.67	12.32	7.95	0	0.92	1.00	4.74	Sa? pec	12.67	1710
44	12257+0713	UGC 07513	12 25 43	+07 13 15	8.88	0.42	5.39	1.71	3	0.66	0.08	7.70	SB(s)cd; sp	13.55	1110
45	12257-1239	NGC 4388	12 25 46	+12 39 22	20.25	0.28	18.10	10.24	0	0.88	0.67	5.39	SA(s)b;sp;Sy2	11.76	2523
46	12261+1306	NGC 4402	12 26 07	+13 06 55	41.60	0.89	17.39	5.32	2	0.94	0.42	7.88	Sb	12.55	232
47	12428-1315	NGC 4639	12 42 53	+13 15 43	5.99	0.45	4.63	1.41	0	0.77	0.42	4.93	SAB(rs)bc;Sy1.8	12.24	1010
48	12437+1623	NGC 4651	12 43 43	+16 23 31	18.99	0.07	15.57	5.45	0	1.00	0.33	4.35	SA(rs)c;LINER	11.39	804
49	12491+0323	NGC 4701	12 49 08	+03 23 04	8.00	0.36	6.32	2.69	2	0.93	0.42	6.49	SA(s)cd	12.80	723
50	13009-0001	NGC 4904	13 00 56	-00 01 57	10.94	0.46	7.14	2.56	1	0.90	0.83	6.61	SB(s)cd	12.6	1168
51	13068-2833	MCG -05-31-035	13 06 51	-28 33 30	4.47	0.27	3.00	1.19	1	0.73	0.03	15.41	SB(rs)d	13.12	2216
52	13088-0646	NGC 4981	13 08 48	-06 46 34	18.57	0.49	11.10	3.51	1	0.91	0.42	8.67	SAB(r)bc;LINER	12.10	1686
53	13110-4435	MCG -07-27-039	13 11 02	-44 35 50	5.58	0.33	1.37	0.28	3	0.77	0.42	10.50	Sb;sp	13.94	4916
54	13128-3241	MCG -05-31-039	13 12 53	-32 41 02	5.22	0.77	2.98	1.06	2	1.09	0.17	8.92	SB(s)dp	13.29	2381
55	13134-7814	MCG +13-10-004	13 13 29	+78 14 17	6.64	0.32	4.98	2.61	1	0.91	0.92	7.29	—	15.7	8837
56	13185-1436	IC 4221	13 18 31	-14 36 17	3.81	0.38	2.55	0.91	3	0.87	0.33	11.25	SA(r)c pec?	13.58	2895
57	13203-2426	NGC 5085	13 20 19	-24 26 06	26.67	0.83	12.90	3.46	2	1.04	1.00	12.34	SA(s)c	12.97	1956
58	13447+5553	UGC 08696	13 44 44	+55 53 31	18.72	0.70	21.38	21.74	0	0.77	1.00	5.70	Sy2;LINER	15.07	11326
59	13477-3056	NGC 5292	13 47 43	-30 56 35	4.97	0.47	2.72	0.71	0	0.95	0.17	9.38	SA(rs)ab	12.84	4466
60	13491+3515	UGC 08739	13 49 11	+35 15 19	18.37	1.07	14.14	6.21	1	0.74	0.83	4.20	SB?	14.57	5032
61	13533+3755	NGC 5351	13 53 21	+37 55 21	3.88	0.41	6.48	1.19	5	0.72	0.50	5.42	SA(r)b	12.98	3610
62	13549+0519	NGC 5356	13 54 58	+05 19 46	5.05	0.14	2.40	0.54	1	0.71	0.17	5.41	SABbc; sp	13.40	1374
63	13550-2646	MCG -04-33-013	13 55 03	-26 46 15	11.62	0.59	6.06	1.68	0	0.73	0.67	12.54	Sa; pec sp	13.35	3455
64	14066-0527	NGC 5468	14 06 36	-05 27 16	10.90	0.56	9.71	3.98	1	0.89	0.17	5.73	SAB(rs)cd	12.41	2845
65	14122+1550	NGC 5504	14 12 15	+15 50 48	4.75	1.33	3.46	1.30	2	0.98	0.17	4.53	SAB(s)bc	13.77	5247
66	14160+3520	NGC 5533	14 16 05	+35 20 15	5.11	0.79	4.05	0.92	1	0.87	0.83	2.32	SA(rs)ab	12.7	3866
67	14247-0313	NGC 5604	14 24 43	-03 13 07	10.47	0.48	7.27	2.77	3	0.89	1.00	8.62	Sa pec?	13.57	2748
68	14429+0453	UGC 09483	14 42 57	+04 53 37	6.81	0.56	5.05	1.71	1	0.78	0.42	6.42	S	13.65	1636
69	14477-1904	NGC 5757	14 47 46	-19 04 30	18.87	0.56	11.77	6.01	1	1.00	1.17	13.18	SB(r)b;HII	13.50	2630
70	15000+0153	NGC 5806	15 00 00	+01 53 22	17.35	0.50	7.88	2.69	0	0.81	0.08	10.83	SAB(s)b	12.4	1359
71	15150+4203	NGC 5899	15 15 00	+42 03 23	22.34	0.65	10.66	3.41	2	0.91	0.83	5.41	SAB(rs)c;Sy2	12.50	2562
72	15349+1144	NGC 5956	15 34 59	+11 44 48	2.22	0.11	1.99	0.55	0	0.67	0.17	5.81	Scd?	13.04	1898
73	15352+3051	NGC 5961	15 35 16	+30 51 57	4.22	0.43	3.25	1.42	2	1.09	0.17	7.06			

Table 4. (continued)

Seq.	Designation ISOSS J	other Name	α_{2000} [h m s]	δ_{2000} [d m s]	$F_{170\mu\text{m}}$ [Jy]	$\Delta_{170\mu\text{m}}$ [Jy]	$F_{100\mu\text{m}}$ [Jy]	$F_{60\mu\text{m}}$ [Jy]	Cirr.	Width [']	Offset [']	$B_{170\mu\text{m}}$ [MJy/sr]	Classification	m [mag]	z [km/s]	
(1)	(2)	(3)	(4)	(5)	(6)	(7)	(8)	(9)	(10)	(11)	(12)	(13)	(14)	(15)	(16)	
86	17493+7009	NGC 6503	17 49 23	+70 09 00	45.49	0.93	25.94	7.58	0	1.03	0.17	5.14	SA(s)cd;HII/LINER	10.91	62	
87	17520+6421	IRAS 17517+6422	17 52 02	+64 21 28	2.92	0.28	3.26	2.22	0	0.77	0.08	6.80	—	—	26151	
88	18118+1459	NGC 6574	18 11 51	+14 59 12	31.89	0.73	27.96	13.22	3	0.77	0.92	17.75	SAB(rs)bc::Sy	12.83	2282	
89	18123+3937	NGC 6585	18 12 21	+39 37 53	7.48	0.51	5.92	2.20	0	1.00	0.08	7.72	S?	13.80	2835	
90	18306+6758	NGC 6667	18 30 39	+67 58 43	8.62	1.46	8.36	2.94	3	0.79	0.92	8.31	SABab? pec	13.55	2582	
91	18335+5953	NGC 6670	18 33 35	+59 53 06	8.64	0.35	15.18	8.24	1	1.09	0.17	6.13	HII	15.70	8684	
92	18526+4244	IRAS 18509+4239	18 52 37	+42 44 21	3.92	0.44	2.10	1.55	6	1.09	0.08	12.81	—	—	12330	
93	19022-5655	IC 4807	19 02 17	-56 55 48	3.04	0.27	2.81	1.05	4	0.85	0.00	8.91	SB(s)c?	14.17	3503	
94	19083+5055	NGC 6764	19 08 19	+50 55 56	13.15	0.44	11.56	6.33	3	0.89	0.75	12.04	SB(s)bc;LINER;Sy2	12.56	2416	
95	19160+6025	NGC 6787	19 16 05	+60 25 02	10.15	0.68	4.36	0.58	5	1.23	0.17	12.20	SAB(s)b	14.70	11790	
96	19215+6108	NGC 6796	19 21 31	+61 08 30	9.16	0.33	10.51	3.82	2	0.69	0.17	7.03	Sbc: sp	13.48	2189	
97	19239-5955	NGC 6782	19 23 57	-59 55 30	5.69	0.46	6.13	2.48	0	1.09	0.08	7.37	SB(r)0/a	11.84	3736	
98	19268+6745	IRAS 19270+6737	19 26 48	+67 45 15	3.19	0.50	2.37	1.17	0	1.18	0.42	8.83	—	—	11410	
99	20047-2625	ESO 200129-2634.2	20 04 45	-26 25 01	3.84	0.28	4.05	2.10	0	0.90	0.33	11.98	—	—	10505	
100	20195+6643	NGC 6911	20 19 34	+66 43 44	17.20	1.70	9.26	3.85	4	0.81	0.83	31.02	SBb:	15.1	2501	
101	20208-4814	NGC 6893	20 20 49	-48 14 24	10.20	1.56	7.31	2.25	1	0.76	0.50	7.09	(L)SA(rs)	12.79	3056	
102	20328+0955	NGC 6928	20 32 50	+09 55 51	9.37	0.41	5.96	1.79	1	0.93	0.25	12.57	SB(s)ab	13.16	4707	
103	20584-4239	ESO 205509-4250.6	20 58 29	-42 39 09	5.40	0.20	9.95	12.78	0	0.81	0.67	6.39	Merger;HII	14.74	12840	
104	21137+1334	NGC 7042	21 13 45	+13 34 34	4.16	0.36	3.14	0.89	1	0.94	0.25	8.22	Sb	12.77	5082	
105	21482+2209	NGC 7137	21 48 14	+22 09 14	10.94	0.78	-1.00	-1.00	-1	0.80	0.33	14.34	SAB(rs)c	13.05	1686	
106	22020-3152	NGC 7172	22 02 01	-31 52 18	13.27	2.03	12.29	5.71	0	0.91	0.25	4.52	Sa pec sp;Sy2	12.85	2603	
107	22078+3121	NGC 7217	22 07 52	+31 21 31	39.18	0.67	18.45	4.96	0	0.93	0.42	10.34	SA(r)ab;Sy	11.02	952	
108	22164-2125	IC 1438	22 16 28	-21 25 37	4.78	0.42	2.61	0.81	1	1.20	0.25	8.29	SAB(r)a	13.19	2616	
109	22494+3454	IRAS 22472+3439	22 49 28	+34 54 42	9.80	0.49	9.90	4.98	0	0.73	0.83	12.34	LINER	16.2	7022	
110	22566-3615	ESO 225349-3631.0	22 56 37	-36 15 05	1.96	0.16	0.75	0.47	0	0.89	0.08	4.84	SB(rs)cd:	13.2	1660	
111	23115+0523	IRAS 23089+0507	23 11 31	+05 23 41	2.74	0.50	2.66	1.15	0	0.86	0.33	11.31	—	—	17.16	14330
112	23147+0431	NGC 7541	23 14 44	+04 31 48	55.82	1.16	40.53	19.31	0	0.77	1.00	6.67	SB(rs)bc: pec	12.42	2678	
113	23161-4234	NGC 7552	23 16 09	-42 34 46	104.66	3.64	101.50	72.03	1	0.87	0.67	5.82	SA(s)c pec;HII	11.25	1585	
114	23210-6913	ESO 231800-6929.4	23 21 01	-69 13 15	9.21	0.22	10.14	5.70	0	0.76	0.83	8.02	—	—	15.99	12513
115	23478-3031	NGC 7755	23 47 51	-30 31 04	12.03	0.38	8.54	2.69	1	1.09	0.92	4.54	SB(r)bc	12.56	2963	

*Table 4 is also available in electronic form at the CDS via anonymous ftp to cdsarc.u-strasbg.fr.

Notes:

- The redshifts for ISOSS J05146-1426, ISOSS J19022-5655, and ISOSS J19160+6025 are from the IRAS PSCz survey (Saunders et al, 2000).
- NGC 0238 (ISOSS J00434-5011) : The identification is neither in the IRAS PSC nor FSC because of insufficient coverage. The IRAS ISSA plate shows clearly a compact source at this position.
- MCG -05-03-020 (ISOSS J00577-2730) : From a second source crossing a well agreeing FCS calibrated flux of 7.9 Jy is derived. A third short slew has only a Default calibration, giving a somewhat lower flux of 3.7 Jy.
- NGC 5356 (ISOSS J13549+0519) : A second slew gave a flux of 8.5 Jy.
- NGC 5985 (ISOSS J15396+5919) : A second slew gave a flux of 22.2 Jy.
- NGC 6787 (ISOSS J19160+6025) : The IRAS 100 μ m flux is an upper limit.
- NGC 7137 (ISOSS J21482+2209) : The identification is neither in the IRAS PSC nor FSC because of insufficient coverage. The IRAS ISSA plate shows clearly a compact source at this position.
- NGC 7217 (ISOSS J22078+3121) : A second slew gave a flux of 57.7 Jy.

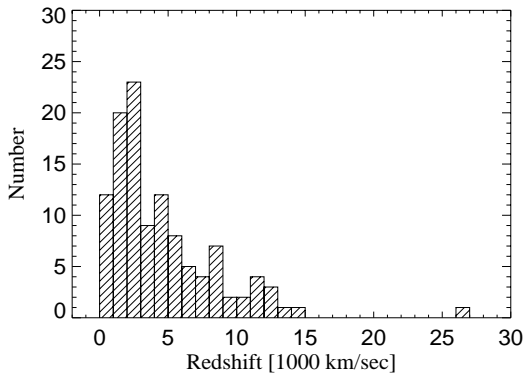


Fig. 4. The redshift distribution of the galaxies from Table 4.

5.2. Redshifts

The redshift distribution (Fig. 4) shows that, although the majority of the sources have low redshifts of $z < 0.02$, our high quality

Serendipity Survey observations also detect galaxies with redshifts up to $z \approx 0.05$. The apparent scarcity of very low redshifts $z < 0.005$ is due to the removal of galaxies with large apparent optical diameters from the list. Since the faintest fluxes of the selected sources reach ≈ 2 Jy, close to the flux density limit of the Serendipity Survey of ≈ 1 Jy (Stickel et al. 1998b), it is expected that the redshift range of the full Serendipity Survey source catalog including sources just above the survey flux limit will not significantly be extended.

5.3. Flux ratios and color temperatures

$F_{170\mu\text{m}} / F_{100\mu\text{m}}$ and $F_{100\mu\text{m}} / F_{60\mu\text{m}}$ flux ratios have been derived for all galaxies except NGC 0238 and NGC 7137, which have no IRAS FSC entry. In a two color diagram $\log(F_{170\mu\text{m}} / F_{100\mu\text{m}})$ vs. $\log(F_{100\mu\text{m}} / F_{60\mu\text{m}})$ (Fig. 5) most galaxies are lo-

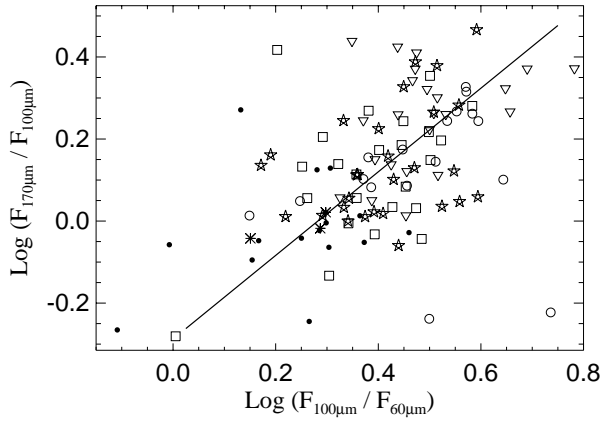


Fig. 5. The two-color $\log(F_{170\mu\text{m}}/F_{100\mu\text{m}})$ vs. $\log(F_{100\mu\text{m}}/F_{60\mu\text{m}})$ scatter diagram. Spiral galaxies are indicated by pentagons, SA type galaxies by open circles, SAB type galaxies by triangles, SB type galaxies by open squares, irregular galaxies by asterisks, and unclassified galaxies by small filled dots. The continuous line is the result of a least squares bisector regression with a slope of ≈ 1 .

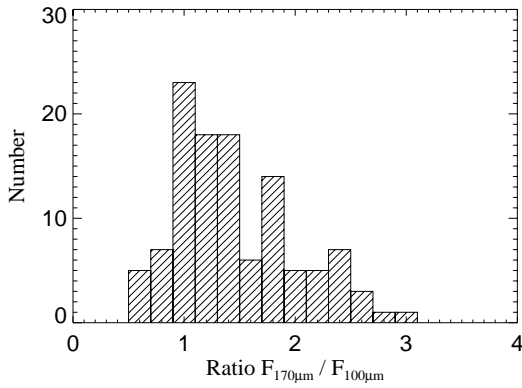


Fig. 6. The distribution of the ratio of Serendipity 170 μm and IRAS PSC 100 μm fluxes.

cated in the region $0.0 \lesssim \log(F_{170\mu\text{m}}/F_{100\mu\text{m}}) \lesssim 0.4$, $0.2 \lesssim \log(F_{100\mu\text{m}}/F_{60\mu\text{m}}) \lesssim 0.6$, with no separation of different Hubble types (S, SA, SAB, SB) noticeable. The FIR spectra of spirals and barred spirals are thus quite similar, indicating no gross differences in the properties of the cold interstellar medium. For the warmer component of the interstellar medium Hawarden et al. (1986) found a clear separation between barred and normal spirals in a $F_{100\mu\text{m}}/F_{25\mu\text{m}}$ vs. $F_{25\mu\text{m}}/F_{12\mu\text{m}}$ diagram, where the excess of the 25 μm flux in barred spirals has been interpreted as enhanced star formation in an inner resonance ring of the bar. For the three irregular galaxies, there appears to be a slight trend that they have smaller values for both flux ratios indicating somewhat warmer dust. Although this is based on a tiny number of objects, it is in accordance with results from IRAS observations (Hunter et al. 1989).

The continuous line in Fig. 5, the ordinary least squares bisector (Isobe et al. 1990), has a slope of 1, representing a linear relationship of $\log(F_{170\mu\text{m}}/F_{100\mu\text{m}}) \propto \log(F_{100\mu\text{m}}/F_{60\mu\text{m}})$.

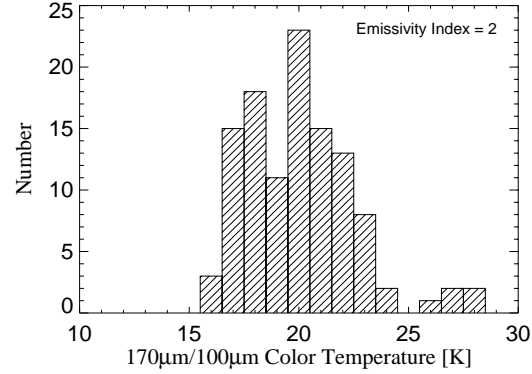


Fig. 7. The color temperature distribution, corrected for the ISOPHOT 170 μm and IRAS 100 μm bandpasses derived using an emissivity index of $\beta = 2$. The broad distribution is centered at $T_D \approx 20$ K, with a range between 15 K and 25 K.

The distribution of $F_{170\mu\text{m}}/F_{100\mu\text{m}}$ flux ratios (Fig. 6) shows that about half of the galaxies have a flux ratio between ≈ 1 and ≈ 1.5 , indicating that the FIR spectra are mostly flat between 100 μm and 200 μm . Very few galaxies show a downward trend in this wavelength range, indicating that their coldest dust component is rather warm with $T_D \gtrsim 25$ K. Most important is the large fraction of more than $\approx 40\%$ of the sources which have $F_{170\mu\text{m}}/F_{100\mu\text{m}} > 1.5$, extending up to $F_{170\mu\text{m}}/F_{100\mu\text{m}} \approx 3$, indicating an up-turn in the SED beyond 100 μm similar to that seen e.g. in the Milky Way and M51 (Chini & Krügel 1993)

This is a clear indication of a cold dust component with dust color temperatures $T_D \lesssim 20$ K in a significant fraction of the galaxies. Since the IRAS as well as the ISOPHOT fluxes refer to a spectrum with $\nu F_\nu = \text{constant}$, dust color temperatures were computed by iteratively correcting the tabulated IRAS FSC 100 μm and ISOSS 170 μm fluxes in the two bandpasses for a modified blackbody (Planck) function

$$F_\nu \propto \nu^\beta B_\nu(T_D), \quad (1)$$

with a fixed emissivity index $\beta = 2$. The resulting distribution of color temperatures (Fig. 7) is centered at $T_D \approx 20$ K, with all but a few sources lying in the range $15 \text{ K} \leq T_D \leq 25 \text{ K}$.

5.4. Total FIR fluxes and luminosities

With the addition of a third flux measurement at 170 μm , the integrated FIR flux F_{40-220} in the wavelength range between 40 μm and 220 μm can be written as

$$F_{40-220} = 1.34 \times 10^{-14} \times [2.58 F_{60\mu\text{m}} + 1.00 F_{100\mu\text{m}} + 0.63 F_{170\mu\text{m}}] \text{ W m}^{-2}, \quad (2)$$

where the relation is valid within $\approx \pm 20\%$ for dust temperatures between 20 K and 80 K and emissivity indices $0 \leq \beta \leq 2$. This formula is similar to the one given by Helou et al. (1988) for the IRAS 60 μm and 100 μm fluxes and extends the coverage to 220 μm assuming a square-wave bandpass 180 μm wide centered at 132.5 μm .

For the general temperature range between 20 K and 80 K, the ratio of F_{40-220} and the total integrated IR flux F_{1-1000}

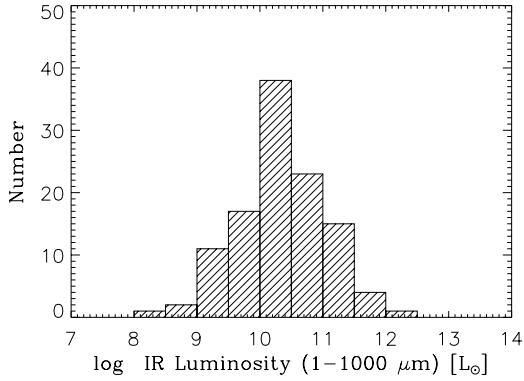


Fig. 8. The IR luminosity distribution, derived from the ISOPHOT Serendipity 170 μm and IRAS 100 μm and 60 μm fluxes. Sources above $10^{12} L_{\odot}$ are usually called ultraluminous.

in the wavelength range between 1 μm and 1000 μm depends rather sensitively on the assumed temperatures and emissivity indices. This reflects the strong dependence on temperature and emissivity indices of the shape of a modified blackbody beyond its peak, which is still covered by the broad ISOPHOT C-160 filter centered at 170 μm .

However, for the coldest dust components with temperatures of 20 K–30 K, with which we are concerned here, the ratio F_{1-1000}/F_{40-220} varies much less and the total integrated IR flux can be written as

$$F_{1-1000} = 1.35 F_{40-220} \text{ W m}^{-2}, \quad (3)$$

which is accurate to within $\approx \pm 30\%$ for emissivity indices $0 \leq \beta \leq 2$.

From the integrated IR fluxes, total IR luminosities L_{1-1000} can be derived by

$$L_{1-1000} = 4 \pi D^2 F_{1-1000}, \quad (4)$$

where D is the luminosity distance. Galaxy distances were computed from the redshifts listed in Table 4 ($H_0 = 75 \text{ km s}^{-1} \text{ Mpc}^{-1}$, $q_0 = 0.5$) for all but the nearby sources with $cz < 800 \text{ km s}^{-1}$, which in turn were taken from the literature. The distribution of L_{1-1000} luminosities (Fig. 8) shows a broad peak at $L_{1-1000} \approx 10^{10.5 \pm 1} L_{\odot}$, covering the range of starburst and luminous infrared galaxies. Very few sources lie close to the border to the ultra-luminous infrared galaxies ($L_{1-1000} \approx 10^{12} L_{\odot}$), only one is above this limit, the well-known ultra-luminous galaxy UGC 8696 (Mkn 273, ISOSS J13447+5553).

5.5. Dust mass

To model far infrared SEDs and calculate dust masses it would be desirable to use properly calculated models derived from radiative transfer codes and detailed grain models. Since the cold dust dominates the total dust mass, a safe lower limit to the dust mass can be obtained by assuming that all the dust grains in the galaxy are at the dust color temperature derived

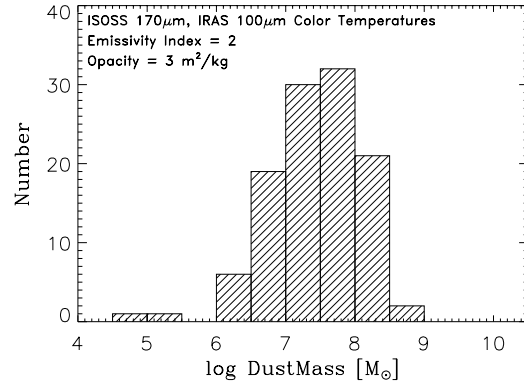


Fig. 9. The distribution of the dust mass, derived from the color corrected dust temperatures with an emissivity index of 2 and a dust opacity of $3 \text{ m}^2/\text{kg}$. The somewhat asymmetric distribution peaks around $M_D \approx 10^{7.5 \pm 0.5} M_{\odot}$. The two sources at the lower end are the only galaxies unambiguously classified as irregulars.

above. The mass of the emitting dust M_D can then be estimated from

$$M_D = D^2 F_{\nu} [\kappa_{\lambda} B_{\nu}(T_D)]^{-1} \quad (5)$$

(Hildebrand 1983; Draine 1990), where κ_{λ} is the dust opacity. A dust opacity of $3 \text{ m}^2/\text{kg}$ was used, which lies in the middle of the range for 170 μm given by Draine (1990). The distribution of dust masses (Fig. 9) is strongly peaked around $M_D \approx 10^{7.5 \pm 0.5} M_{\odot}$. These dust masses are a factor 2–10 larger than those derived from IRAS 60 μm and 100 μm fluxes alone, and reach values which have been found for a few other galaxies only by including a very cold dust component inferred from sub-mm measurements (Krügel et al. 1998; Siebenmorgen et al. 1999).

There appears to be a sharper drop-off towards higher dust masses compared to the lower dust masses, which decline more gradually. There are two sources having only $\approx 1\%$ of the average dust mass, namely the only two galaxies unambiguously classified as irregulars galaxies (UGC 2238, NGC 3077).

Alternatively, dust masses for a fixed emissivity index $\beta = 2$ can be computed from

$$M_D = 7.9 \cdot 10^3 \frac{L_{1-1000}}{10^8 L_{\odot}} \left(\frac{T_D}{40 \text{ K}} \right)^{-6} M_{\odot}. \quad (6)$$

This assumes standard grain properties (radius 0.1 μm , density 3 g cm^{-3} ; Hildebrand 1983) and extends the formula given by Klaas & Elsässer (1993).

Overall, the distribution of dust masses derived from the total IR luminosity L_{1-1000} (Eq. (6)) is very similar to that from the 170 μm Serendipity fluxes (Eq. (5), Fig. 9,) alone. On average, the former are $\approx 50\%$ smaller than the latter.

Fig. 10 shows the distribution of the dust masses from Fig. 9 separately for different Hubble types. There is again no obvious difference between the normal spiral and the barred spiral galaxies. Only the two galaxies unambiguously classified as irregulars have a significantly lower dust mass. Galaxies without a morphological classification are preferentially located at the

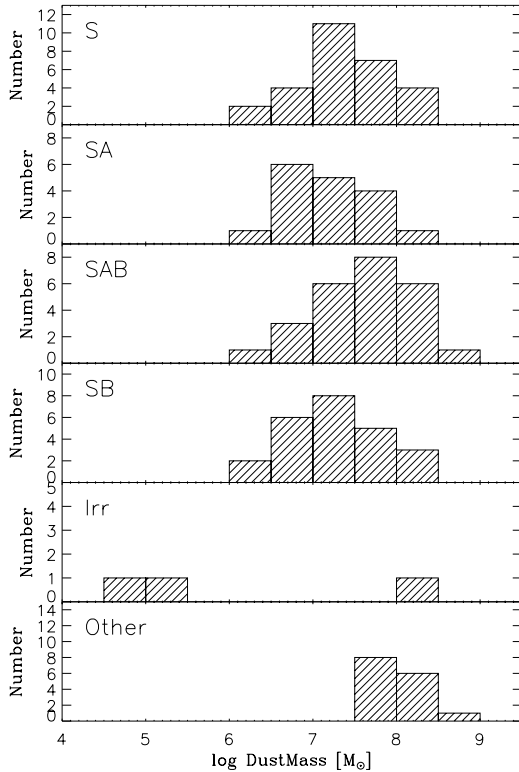


Fig. 10. The distribution of the dust mass for the different galaxy Hubble types. Galaxies without a morphological classification as spiral, barred spiral, or irregular are shown in the lower panel. The classification of the irregular galaxy with the highest dust mass is uncertain.

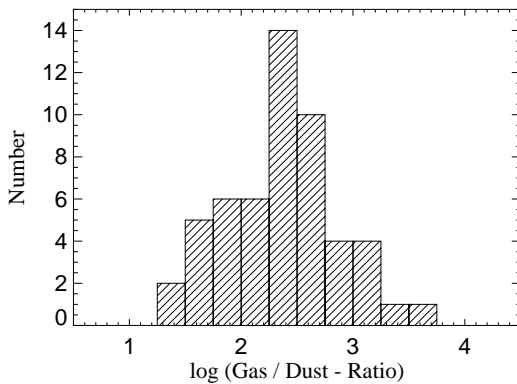


Fig. 11. The distribution of the gas-to-dust ratio peaks at ≈ 250 , close to the canonical value for the Milky Way.

high end of the dust mass distribution, which simply reflects the fact that they comprise the subgroup with the highest redshifts, where a classification needs a detailed optical investigation. In fact, the redshifts of sources in this group are generally higher than 7000 km s^{-1} , while almost all other galaxies are at smaller redshifts.

5.6. Gas-to-dust ratio

Gas masses from HI measurements, occasionally supplemented by H_2 masses derived from CO measurements, have been found

in the literature for about half of the 115 Serendipity sources. The gas-to-dust ratio distribution (Fig. 11) shows a broad peak with a median value of ≈ 250 , very close to the canonical value of the Milky Way (≈ 160). This indicates for the first time that the gas-to-dust ratio found for the Milky Way also applies to other external galaxies, and that there is at least some justification in using this value to convert FIR measured dust masses to total gas masses. However, the derived gas-to-dust ratios cover the large range between ≈ 50 and ≈ 1000 . From IRAS data alone, a range between ≈ 500 and ≈ 2000 had been found, with an average of ≈ 1000 (Devereux & Young 1990). Although the average of the gas-to-dust ratio with dust masses from the 170 μm Serendipity Survey fluxes is close to the galactic value, the spread is nevertheless large, likely larger than expected from errors in the FIR fluxes or gas masses. This can be taken as evidence that the spread of the gas-to-dust ratio reflects a property of the galaxy populations in the sample and that there is no fiducial gas-to-dust ratio applicable to all normal late type galaxies. This might be due to the different galaxy morphologies, could possibly be also an age effect from the continuous transformation of gas into dust via the stellar evolution, or be related to the overall metallicity of the galaxies.

6. Conclusions

The ISOPHOT Serendipity Survey 170 μm data taken during the slewing of the ISO telescope have been used to establish a first list of compact high quality sources located on a low cirrus background at high galactic latitudes. A total of 115 sources satisfied the rather stringent selection criteria. The total 170 μm fluxes for the vast majority of the sources have been measured for the first time.

The raw Serendipity Survey fluxes are tied to an absolute flux level by using a total of 12 repeatedly crossed sources as standards, which were also measured with ISOPHOT's photometric mapping mode. The ratio between the slew and mapping fluxes is used to derive a scaling correction for the raw Serendipity fluxes, which is brightness dependent for raw slew fluxes up to $\approx 30 \text{ Jy}$, and constant for higher fluxes. The scatter in the ratio between the slew and mapping fluxes indicates that a photometric accuracy of $\lesssim 40\%$ is achieved. From the comparison of the Serendipity slew positions with optical positions, a positional accuracy of $\approx 45''$ was found.

The observed 170 μm fluxes lie in the range $2 \lesssim F_{170\mu\text{m}} \lesssim 100 \text{ Jy}$, the redshifts reach out to $z \approx 0.05$. Supplementing the Serendipity Survey 170 μm with IRAS 100 μm fluxes, the flux ratio $F_{170\mu\text{m}}/F_{100\mu\text{m}}$ indicates that about half of the galaxies have a flat FIR spectrum between 100 μm and 200 μm . However, a large fraction of more than 40% of the sources show an upward trend in their FIR spectra, with $F_{170\mu\text{m}}/F_{100\mu\text{m}}$ ratios of up to 3. Integrated IR luminosities shows a broad peak at $L_{1-1000} \approx 10^{10 \pm 1} L_{\odot}$ characteristic of starburst and luminous infrared galaxies.

Correcting the 100 μm and 170 μm fluxes for the band-passes and using an emissivity index of $\beta = 2$, a dust color temperature distribution centered at $\approx 20 \text{ K}$ is found, where all

but a few sources lie in the range $15 \text{ K} \leq T_D \leq 25 \text{ K}$. For the first time this indicates that a cold dust component with $T_D \leq 20 \text{ K}$ is present in a large fraction of all spiral galaxies. Dust masses based on the 170 μ m fluxes and these color temperatures cover a wide range between $\approx 10^6 M_\odot$ and $\approx 10^{8.5} M_\odot$. Together with published gas masses, mainly from HI observations, these dust masses result in a broad gas-to-dust ratio distribution peaking at ≈ 250 , close to the canonical value for the Milky Way. Although this shows that gas-to-dust ratios similar to that of the Milky Way are also found in a significant number of other galaxies, the wide range may also be taken as evidence for significant differences among the galaxies in the presented sample.

By relaxing the selection criteria, it is anticipated that 170 μ m fluxes for a much larger number of galaxies, possibly more than 1000 sources, will become available. This large database is expected to put the described initial results on a much broader basis and will also allow to find possibly rare classes of extragalactic FIR emitters.

Acknowledgements. The ISOPHOT project was funded by Deutsches Zentrum für Luft- und Raumfahrt (DLR, formerly DARA), the Max-Planck-Gesellschaft, the Danish, British, and Spanish Space Agencies and several European and American institutes. This research has made use of the Digitized Sky Survey, produced at the Space Telescope Science Institute, NASA's Astrophysics Data System Abstract Service, the Simbad Database, operated at CDS, Strasbourg, France, and the NASA/IPAC Extragalactic Database (NED) which is operated by the Jet Propulsion Laboratory, California Institute of Technology, under contract with the National Aeronautics and Space Administration. We thank Th. Ochotta for screening the literature and collecting the gas masses.

References

- Acosta-Pulido J.A., Gabriel C., Castañeda H.O., 2000, *Experimental Astronomy*, in press
- Alton P.B., Trehella M., Davis J.I., et al., 1998, *A&A* 335, 807
- Bogun S., Lemke D., Klaas U., et al., 1996, *A&A* 315, L71
- Chini R., Krügel E., 1993, *A&A* 279, 385
- Chini R., Krügel E., Lemke R., Ward-Thompson D., 1995, *A&A* 295, 317
- Draine B.T., 1990, in: Thronson H.A.Jr., Schull J.M. (eds.), *The Interstellar Medium in Galaxies*. Dordrecht: Kluwer, p. 483
- Devereux N.A., Young J.S., 1990, *ApJ* 359, 42
- Gabriel C., Acosta-Pulido J., Heinrichsen I., et al., 1997, *Astronomical Data Analysis Software and Systems VI*, in: Hunt G., Payne H.E. (eds.), *A.S.P. Conference Series* 125, p. 108
- Haas M., 1998, *A&A* 337, L1
- Haas M., Lemke D., Stickel M., et al., 1998, *A&A* 338, L33
- Hawarden T.G., Mountain C.M., Leggett S.K., Puxley P.J., 1986, *MNRAS* 221, 41P
- Helou G., Khan I.R., Malek L., Boehmer L., 1988, *ApJS* 68, 151
- Hildebrand R.H., 1983, *QJRAS* 24, 267
- Hook R.N., Fruchter A.S., 1997, *Astronomical Data Analysis Software and Systems VI*, in: G. Hunt G., Payne H.E. (eds.), *A.S.P. Conference Series* 125, p. 147
- Hunter D.A., Gallagher J.S.III, Rice W.L., Gillett F.C., 1989, *ApJ* 336, 152
- Isobe T., Feigelson E.D., Akritas M.G., Babu G.J., 1990, *ApJ* 364, 104
- Imme M., 1991, *CVGIP: Graphical Models and Image Processing* 53, 204
- Kessler M.F., Steinz J.A., Anderegg M.E., et al., 1996, *A&A* 315, L27
- Klaas U., Elsässer H., 1993, *A&A* 280, 76
- Klaas U., Krüger H., Heinrichsen I., Heske A., Laureijs R.J., 1994, *ISOPHOT Observers Manual (Ver. 3.1)*, Noordwijk: ISO Science Operations Team (ESA/ESTEC)
- Klaas U., Haas M., Heinrichsen I., Schulz B., 1997, *A&A* 325, L21
- Krügel E., Siebenmorgen R., Zota V., Chini R., 1998, *A&A* 331, L9
- Lemke D., Klaas U., Abolins J., et al., 1996, *A&A* 315L, 64
- Mathis J.S., 1990, *ARA&A* 28, 37
- Moshir M., Kopan G., Conrow T., et al., 1992, *Explanatory Supplement to the IRAS Faint Source Survey, Version 2 (Pasadena: JPL)*
- Odenwald S., Newmark J., Smoot G., 1998, *ApJ* 500, 554
- Perez Garcia A.M., Rodriguez Espinosa J.M., Santolaya Rey A.E., 1998, *ApJ* 500, 685
- Saunders W., Sutherland W.J., Maddox S.J., et al., 2000, *astro-ph/0001117*, submitted to *MNRAS*
- Schlegel D.J., Finkbeiner D.P., Davies M., 1998, *ApJ* 500, 525
- Siebenmorgen R., Krügel E., Chini R., 1999, *A&A* 351, 495
- Smith J., 1982, *ApJ* 261, 463
- Smith S.M., Brady J.M., 1997, *Int. Journal of Computer Vision* 23, 45
- Stark A.A., Davidson J.A., Platt S., et al., 1989, *ApJ* 337, 650
- Sternberg S., 1986, *Computer Vision, Graphics and Image Processing* 35, 333
- Stickel M., Bogun S., Lemke D., et al., 1998a, *A&A* 336, 116
- Stickel M., Lemke D., Bogun S., et al., 1998b *"ISOPHOT far-infrared serendipity sky survey"*, *Proc. SPIE* 3349, p.115
- Stickel M., Lemke D., Bogun S., et al., 1999, *The ISOPHOT far-infrared serendipity sky survey*, in: Cox P., Kessler M.F. (eds.), *The Universe as seen by ISO, ESA SP 427*, p. 839